Effects of trapping site on the spectroscopy of $^1P_1$ excited group 12 metal atoms in rare gas matrices

Cite as: Low Temp. Phys. **45**, 697 (2019); https://doi.org/10.1063/1.5111289
Published Online: 23 July 2019

M. Lara-Moreno, J. Alvarez-Hernández, H. Negrín-Yuvero, J. G. McCaffrey, and G. Rojas-Lorenzo

Low Temperature Physics ARTICLE scitation.org/journal/ltp

Effects of trapping site on the spectroscopy of $^1P_1$ excited group 12 metal atoms in rare gas matrices

Cite as: Fiz. Nizk. Temp. **45**, 816–826 (July 2019); doi: 10.1063/1.5111289
Submitted: 24 May 2019

M. Lara-Moreno,[1,2] J. Alvarez-Hernández,[1,3] H. Negrín-Yuvero,[1] J. G. McCaffrey,[4] and G. Rojas-Lorenzo[1,a)]

AFFILIATIONS

[1]Instituto Superior de Tecnologías y Ciencias Aplicadas (InSTEC), Universidad de La Habana Ave. Salvador Allende No. 1110, Quinta de los Molinos, La Habana 10400, Cuba
[2]Université de Bordeaux and CNRS, ISM, UMR 5255, F-33400 Talence, France
[3]Department of Chemistry, University of Rochester, Rochester, USA
[4]Department of Chemistry, Maynooth University, National University of Ireland Maynooth, County Kildare, Ireland

[a)]**E-mail:** german@instec.cu

ABSTRACT

A molecular dynamics deposition model has been used to simulate the growth of rare gas matrices doped with atoms of the group 12 elements zinc, cadmium and mercury. This study investigates the sites occupied by Zn, Cd and Hg metal atoms when isolated in the solid rare gases. To probe the results, the resonance $^1P_1 \leftarrow ^1 S_0$ transitions of the matrix-isolated metal atoms were calculated and compared with the recorded spectra of the M/RG solids. The theoretical spectroscopy obtained in this work was generated using the molecular dynamics with quantum transitions method. In Ne matrices the metal atoms preferably occupy tetra- and hexa-vacancy sites while in the case of Xe matrices, only the single vacancy site is formed. For Ar and Kr matrices Zn but especially Cd can be trapped in tetra- and hexa-vacancy sites in addition to single-vacancy sites, while Hg atoms show exclusive occupancy in single vacancy sites.

1. INTRODUCTION

Photo-induced processes in metal atoms have been studied for some decades owing to their importance in the development of optoelectronic devices like excimer lasers. Matrix-isolation, specifically using rare gas solids as host materials, is an experimental technique that provides one of the most useful model systems to explore such phenomena. Despite the existence of numerous experimental studies that have been conducted in these model solids,[1–7] the site occupied by the guest metal atom still represents one of the major unknowns in matrix-isolation spectroscopy. As site occupancy is essential for understanding the complex dynamics of the trapped guest in its excited states, we have pursued the group 12 elements Zn, Cd and Hg since these metal atoms have been the subject of detailed experimental studies, most notably using excitation spectroscopy.

Usually, substitution of a host rare gas atom by a guest atomic species is assumed in matrix studies of most metals. However, this approach is not adequate to account for the experimental findings made for most systems. For example, the existence of multiple trapping sites for alkali atoms in rare gas matrices is now a well-accepted concept in the matrix-isolation literature.[6–8] In order to identify the trapping sites of atomic Li in neon matrices, Fajardo[6] developed specific experiments and Monte Carlo simulations. This study revealed that tetrahedral and octahedral sites are the most stable ones in neon matrices. These configurations arise as a result of the removal of four or six neon atoms from the host lattice and the voids thereby created can then accommodate the guest Li atom. A more recent theoretical study[8] has focused on the spectroscopic properties of alkali atoms (Li, Na, K), embedded in Ar solids using a model based on core polarization pseudopotentials. This investigation shows that essentially two crystal sites are stable and both contribute to the spectroscopic patterns of these matrices. The proposed sites are single-vacancy (*sv*), with cubic (O_h) symmetry, and tetra- vacancy (*tv*) with tetrahedral (T_d) symmetry.

The Maynooth Group have utilized excitation spectroscopy, recorded by monitoring site-specific emission — both steady-state and time-resolved, to resolve features in strongly congested absorption spectra which arise from multiple site occupancies.[1,2,4] Compounding this complexity, luminescence spectra recorded for the resonance $^1P_1 \rightarrow ^1 S_0$ transition of the metal atoms Zn and Cd trapped in the heavier rare gas matrices revealed the existence of pairs of emission bands which are attributed to a single thermally

stable site. Careful annealing and excitation spectroscopy conclusively demonstrated that the existence of pairs of emission bands, which are best illustrated by the Zn/Ar system, are not an effect of multiple site occupancy but rather a result of the Zn atom being trapped in a single site. To analyze and interpret this complex behavior it is essential to achieve confident assignments for the sites occupied by these metal atoms in the rare gas solids.

Initial experimental studies by the Maynooth Group focused on the metal (M) atoms Zn, Cd and Hg isolated in rare gas (RG) solids Ne, Ar, Kr and Xe since it was known that the ground state bond lengths in the 1:1 M-RG complexes matched, with the exception of M-Ne, the sizes of single vacancy (*sv*) sites. Favorable comparison with spectral simulations based on localized interactions limited to M-RG_{18} complexes, suggested that the guest metal atom occupies the same *sv* sites in the three heaviest host matrices. Site occupancy of these metal atoms in neon becomes more complex[1] for which tetra-vacancy (*tv*) and hexa- vacancy (*hv*) sites had also to be taken into account. Comparing the interatomic distances of each site with the gas phase diatomic potentials, Healy *et al.* concluded that the bands identified in the M/Ne matrix data are best attributed to *tv* and *hv* sites.[1] A graphical representation of interatomic pair potentials, describing the ground state M($^1S_0$)-RG interactions for the three group 12 metal atoms and the four rare gases is shown in Fig. 1. Also shown there (by the solid black traces) are the rare gas dimer potentials for Ne-Xe.

As the comparison provided in Fig. 1 reveals, M-Ne interactions are much weaker than in the other M-RG diatomics but more significantly for the site occupancy of guest metal atoms in solid neon, the attractive parts of these potentials all occur at much greater distance than in neon dimer. It is also evident that the strength of the M-RG interactions increases steadily as the mass of the RG increases. Indeed, for the M-Xe interactions, greater binding energies exist than in xenon dimer at bond lengths very similar to or even less than (in the case of Hg) the rare gas dimer. Regarding the metal atom, it is clear in Fig. 1 that Hg always has the shortest bond length of the three group 12 metal atoms. This is an illustration of the "lanthanide contraction" in neutral species, a characteristic that is well documented in the ionic radii of these elements.

With regard to site occupancy, a conclusion that can be drawn from Fig. 1 is that the metal atoms are unlikely to be trapped in *sv* sites in Ne matrices for which the most probable sites are *tv* and *hv*. Hg atoms could be trapped in *sv* sites for all matrices except Ne. However, it is not clear whether Zn atoms are trapped in a *sv* site in Ar matrices. The equilibrium distance for the Zn-Ar interaction is in between the nearest neighbor distances of a *sv* and *tv* sites.

In Kr matrices Zn and Hg atoms could be trapped in *sv* sites, while Cd atoms shows a similar situation to Zn atoms in Ar matrices. According to Fig. 1, all metal atoms that we have considered could be potentially trapped in *sv* sites in Xe matrices.

Theoretical deposition models[7,9–14] have been shown to be a useful and reliable tool in order to assess the formation of trapping sites in rare gas solids doped with atomic and molecular impurities. They allow not only the identification of trapping sites, but also a geometrical analysis of the environment which surround the trapped species. In the present work, molecular dynamics (MD) is employed to simulate the formation of doped rare gas matrices, thus allowing an investigation of the guest site occupancy. We have specifically focused on the study of the zinc, cadmium and mercury trapped in the rare gases neon, argon, krypton and xenon matrices because the matrix absorption and excitation spectra of these metal atoms is well documented. Accordingly, the electronic $^1P_1 \rightarrow {}^1S_0$ transition of the metal atoms trapped in the *sv*, *tv* and *hv* sites are calculated for zinc and cadmium using molecular dynamics with quantum transitions (MDQT).[15] Results for the corresponding

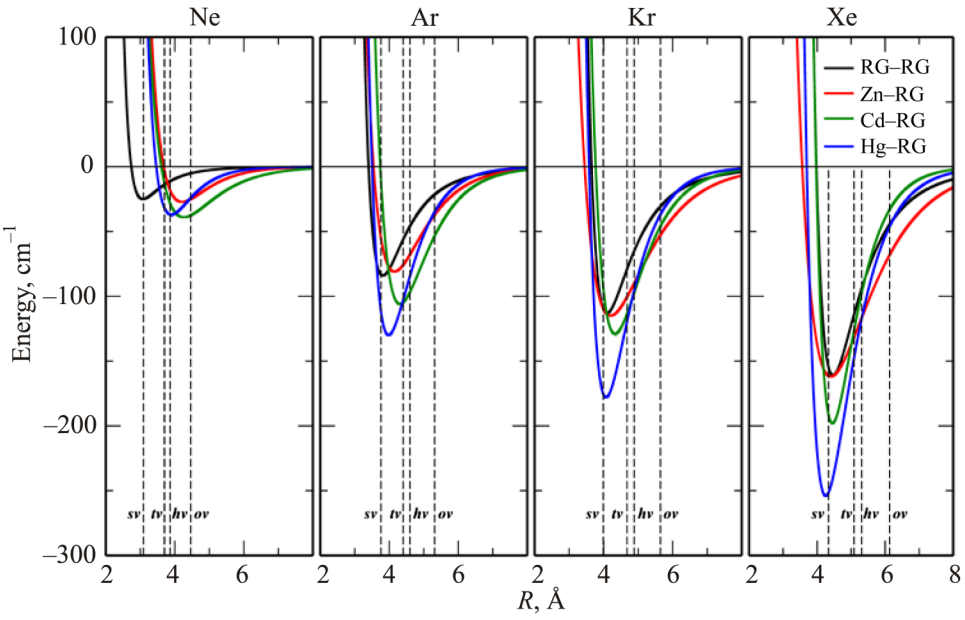

FIG. 1. Comparison of the ground state interatomic M($^1S_0$)–RG (colored coded traces) and RG–RG (black traces) pair-potentials. The broken vertical lines represent interatomic distances of the *sv*, *tv*, *hv* and *ov* (octahedral) vacancy sites in the solid rare gases Ne, Ar, Kr and Xe.

$^1P_1 \rightarrow {}^1S_0$ transition of atomic mercury trapped in the *sv* site have already been determined with this method[16] and for that reason are not repeated here. Finally, the results of the deposition model are used to weight the contributions of each site to the spectrum.

2. METHODS

2.1. Deposition simulations

The methodology used in the present calculations to simulate sample deposition is the same as that described by Crepin *et al.*[7,11,14] Briefly, the growth of the crystal was simulated by MD calculations starting from an atomic template that mimics the geometrical properties of the solid. The Verlet algorithm was used to integrate the equations of motion using time steps of 10 fs. The RG-RG and M-RG interactions were, respectively, described by Lennard-Jones and Morse interatomic pair potentials[17–25] shown in Fig. 1 and whose parameters are collected in Table I. The starting configuration (framework) was built using 288 RG atoms which represents 4 atomic layers (72 atoms per layer) each with an edge length of 6ax6a, where *a* is the lattice parameter of the pure rare gas solid. The atomic layers were ordered along the z axis. The lowest layer has all atoms frozen at their equilibrium positions to avoid surface effects and to prevent translational and rotational motions during the deposition process. The next layer acts as a thermostat whereby the velocities of its atoms are rescaled at each MD time step, in order to keep the temperature fluctuating around the desired value. The atoms of the next two layers are free to move under a classical force field.

The framework is initially equilibrated to the desired temperature before starting the growing process. Then, every 5 ps a RG atom is shot to the template, with an initial thermal velocity, from a distance greater than 8*a* from the upper layer, to avoid any initial interactions between the projectile (an atom) and the atoms of the target (the framework). The atom is captured by the surface and the collision energy is transferred to the system and distributed among all degrees of freedom of the solid. The lattice growth is thereby achieved by the collision of 576 RG atoms which generates a system with 12 layers (864 atoms).

The projectiles started their movement along the *z* direction with uniform random values for *x* and *y* coordinates enclosed inside a surface with $6a \times 6a$ dimensions, to ensure the proper covering of the framework. Periodic boundary conditions were applied along the *x* and *y* directions, but not along the *z* direction. The fcc structure was used as the atomic framework in two orientations. One had the layers oriented parallel to (100) crystallographic plane while the other one had the atomic layers oriented parallel to the (111) plane. The results obtained in both orientations were similar.

This process was applied to simulate the growth of Ne, Ar, Kr and Xe matrices doped with Zn, Cd and Hg atoms. The depositions were simulated at two different temperatures, 4 and 10 K in order to account for the annealing effects observed for the thermally unstable vacancy sites described in experiments.[1–4] About 1000 simulations of the deposition were performed to perform statistical analysis.

The deposition model applied in this work has been proposed and used successfully by other authors trapping atoms and molecules in rare gas solids.[7,11,14] The 6*a* length guarantees to provide a cut-off radius in a region where interactions M-RG are negligible.

2.2. Potential energy surfaces for the $^1P_1$ electronic state

The initially degenerate $^1P_1$ electronic state of the Zn and Cd atoms becomes non-degenerate after the interaction with the RG therefore giving rise to two electronic states $^1\Pi$ and $^1\Sigma$ for the diatomic M-RG complex. The resulting $^1\Pi$ state differs from $^1\Sigma$ state by the projection of the angular momentum onto the interatomic axis. The repulsive $^1\Sigma$ state is associated with the projection $\Omega = 0$ of the metal atom electronic angular momentum $J = 1$ onto the interatomic axis. Correspondingly, the attractive $^1\Pi_1$ state of the

TABLE I. The parameters D_e (cm^{-1}), R_e (Å) and β ($Å^{-1}$) of Morse functions $D_e[1 - e^{-\beta(r-R_e)}]^2 - D_e$, used to represent the ground-state potential energy curves for the 12 M–RG diatomics considered in this study. Lennard-Jones (LJ) potentials $4\varepsilon 0\ [(\sigma/r)^{12} - (\sigma/r)^6]$ are used to describe the 4 RG–RG interactions in solid neon, argon, krypton and xenon. The values used for ε_0 (cm^{-1}) and σ (Å) are from Ref. 25.

M→	Zn			Cd			Hg			LJ	
RG ↓	D_e	R_e	β	D_e	R_e	β	D_e	R_e	β	ε_0	σ
Ne	27.2[a,b]	4.21[a,b]	1.310[a,b]	39.0[a,b]	4.26[a,b]	1.060[a,b]	37.0[g]	3.90[g]	1.586[g]	25	2.74
Ar	80.9[a,b]	4.15[a,b]	1.146[c]	106.0[a,e]	4.31[a,e]	1.213[a,e]	130.0[h]	3.98[h]	1.448[h]	84	3.40
Kr	115.0[d]	4.20[d]	0.922[d]	129.0[e]	4.33[e]	1.233[e]	178.0[i]	4.07[i]	1.405[i]	113	3.65
Xe	162.0[c]	4.40[c]	0.828[a,c]	198.0[f]	4.45[f]	1.450[f]	254.0[h]	4.25[h]	1.249[h]	161	3.98

[a]Value changed within the interval of uncertainty reported in the reference.
[b]Reference 17.
[c]Reference 18.
[d]Reference 19.
[e]Reference 20.
[f]Reference 21.
[g]Reference 22.
[h]Reference 23.
[i]Reference 24.

TABLE II. Parameters of Morse $D_e\,[1-e^{-\beta(r-R_e)}]^2$ and anti-Morse 5/2 $D_e\,[1+e^{-\beta(r-R_e)}]^2$, functions used to represent the molecular potential energy curves V_Σ and V_Π for M(Zn, Cd)–RG interactions: D_e (cm^{-1}), R_e (Å) and β ($Å^{-1}$). Parameters of repulsive function Ae^{-br} describing potential V_Σ for Zn–Xe: A (10^6 cm^{-1}) and b ($Å^{-1}$).

M→	Zn					Cd		
RG–M ↓	D_e	R_e	β	A	b	D_e	R_e	β
Ne–M($^1\Pi$)	81.0[c]	3.48[c]	1.360[c]	—	—	89.0[f]	3.61[f]	1.240[f]
Ar–M($^1\Pi$)	508.5[d]	2.99[d]	1.264[d]	—	—	518.5[f]	3.28[f]	1.399[f]
Kr–M($^1\Pi$)	1400.0[e]	2.80[e]	1.594[e]	—	—	1036.0[f]	3.17[f]	1.524[f]
Xe–M($^1\Pi$)	3241.0[e]	2.83[e]	1.649[e]	—	—	—	—	—
Xe–M($^3\Pi$)	1400.0[e]	3.00[e]	1.750[e]	—	—	—	—	—
Ne–M($^1\Sigma$)	81.0[a]	3.48[a]	1.360[a]	—	—	89.0[a]	3.61[a]	1.240[a]
Ar–M($^1\Sigma$)	42.8[d]	6.38[d]	0.680[b]	—	—	11.5[g]	7.30[g]	0.670[b]
Kr–M($^1\Sigma$)	64.0[c]	6.30[c]	0.630[c]	—	—	21.0[g]	7.04[g]	0.663[g]
Xe–M($^1\Sigma$)	—	—	—	1.000[e]	1.725[e]	—	—	—
Xe–M($^3\Sigma$)	—	—	—	1.079[e]	1.700[e]	—	—	—

[a]The potential was represented as anti-Morse function.
[b]The β coefficient was varied to obtain a more repulsive wall in the energy potential curve.
[c]Reference 27.
[d]Reference 28.
[e]Reference 29.
[f]Reference 20.
[g]Reference 30.

M-RG complex is associated with the quantum numbers $|J=1, \Omega=\pm 1>$. For the ^{1}P state there is no further mixing due to the spin-orbit coupling, so pure Σ and Π molecular states arise.

The potential energy curves of the $^1\Sigma$ and $^1\Pi$ molecular states [$V_\Sigma(R)$ and $V_\Pi(R)$] have been deduced from both experimental and theoretical methods.[17–32] In the present study they are represented by Morse or anti-Morse potentials whose parameters are collected in Table II.

The total interaction Hamiltonian, H^{M-RG}, for the electronic states correlating with the metal atom states M($^1S_0$) or M($^1P_1$) is obtained as the sum of pairwise interactions:

$$H^{M-RG} = \sum_{k=1}^{n_{RG}} H^{M-RG_k}, \tag{1}$$

where n_{RG} is the number of rare gas atoms in the system and H^{M-RGk} is the diatomic interaction Hamiltonian of the diatom formed by the metal atom and the kth rare gas atom.

Due to the isotropic nature of the interactions with the $^1S_0$ metal atom, the ground state energies are obtained from Eq. (1) by simple summation. In the excited states, the H^{M-RG} Hamiltonian is built from the potentials of the Σ and Π orientations of the M–RG diatom. However, this Hamiltonian is only diagonal in the reference frame (x,y,z) of the diatom with the z axis parallel to the internuclear M–RG_k axis. In order to obtain the matrix elements of the Hamiltonian in the laboratory frame a series of rotations must be performed as described by Batista and Coker.[32,33] Then, the resulting H^{M-RG} matrix is diagonalized in order to obtain the adiabatic energies E_i. Details of the practical implementation of this procedure are given in the appendices of Refs. 15 and 34. Three PESs are thus obtained from these energy calculations for the configurations of interest. Each PES correspond to a given electronic adiabatic state of the system.

2.3. Spectral simulations

The calculations described in this work were carried out with a minimum image convention model of the system which consist of one metal atom, either Zn or Cd, and an arrangement of 500 rare gas atoms in a box large enough to avoid size effects (at least for the short timescales of the dynamical simulations). The metal atom was initially placed in three different vacancy sites of the solid rare gas hosts: namely *sv*, *tv*, and *hv*. These three sites were chosen according to previous theoretical and experimental reports[1,6,8] and are presented in Fig. 2. No MDQT simulations with Hg atoms were performed.

As the first step in our calculations, the system was equilibrated in the electronic ground state at an effective temperature, T_0. The last 100 ps of the thermalization step were used to collect a set of initial positions and momenta (configurations) for the subsequent spectral simulations. The stored configurations fulfill the classical Franck-Condon principle for the electronic transition at the excitation wavelength (λ_{ex}) from the ground state to one of the three possible adiabatic excited states asymptotically correlated to the metal atom $^1P_1$ state. Each excitation event can reach any of the excited states and for this reason, the initial populations produced of the three excited states were taken to be equal.

One hundred trajectories each of 20 ps duration were run from these initial configurations by Franck-Condon switching to each of the three excited states. The propagation time (20 ps) was sufficient to achieve not only convergence of the final electronic state populations but also the minimum energy configuration. In

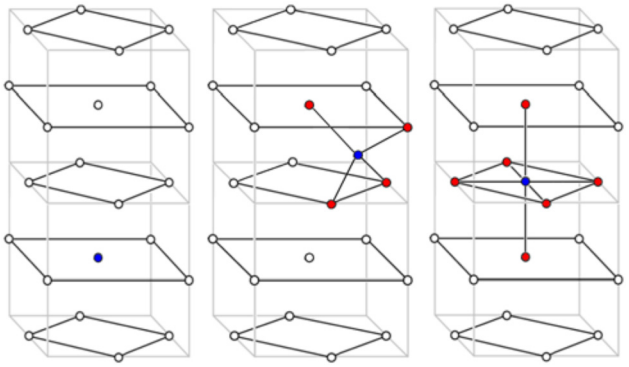

FIG. 2. Models of the three vacancy sites considered in this work. Shown from left to right are the single vacancy *sv*, tetra-vacancy *tv* and hexa-vacancy *hv* sites. The empty circles represent RG atoms in the fcc lattice, the blue circles show the position of the guest M atom in each model while the red circles indicate the locations of the removed RG atoms forming the specific vacancy. The octahedral vacancy (*ov*) site mentioned in Fig. 1 is not shown. It corresponds to the removal of 12 RG atoms surrounding the guest metal atom. In this diagram it would correspond to the removal of all the RG atoms surrounding the metal atom in the bottom of the structure shown in left panel of the figure.

order to represent the vibrational amplitudes of the RG atoms, we adjusted their velocities to an effective temperature T_0 estimated with two procedures: namely the harmonic approximation described by Bergsma *et al.*[35] and the anharmonic approximation described by Uranga *et al.*[36] The trajectories were run at effective constant temperatures of 17, 49, 36 and 32 K for Ne, Ar, Kr and Xe matrices, respectively. These temperatures are chosen so that the classical probability distribution for the motion of the lattice atoms at T_0 equals the quantum probability distribution at the actual experimental temperature of 4 K.

3. RESULTS AND DISCUSSION

3.1. Site occupancy

The results obtained from the simulated depositions demonstrated the formation of all three proposed vacancy sites illustrated in Fig. 2, namely *sv*, *tv*, and *hv*. The probabilities of occurrence of each vacancy site are given in Table III for both 4 and 10 K depositions. In the case of Ne matrices, multiple vacancy sites are present even for the higher temperature for all three metals. The simplest of the M/Ne systems is Hg/Ne where the *tv* site dominates. In the other neon matrices roughly equal amounts of *tv* and *hv* sites are found for both Cd and Zn atoms. *Sv* site occupancy does not occur for any of the three group 12 metal atoms in solid neon. The 0.9% found in Zn/Ne deposited at 10 K is absent at 4 K and is thereby considered negligible.

In sharp contrast, single vacancy site occupancy plays a dominant role for the site of isolation of these metal atoms in the heavier solid rare gases. For atomic zinc and mercury, it is the only site formed for all three solids, except Zn/Kr where the *tv* site exists in a tiny amount of 0.3%. Cd/Ar and Cd/Kr present the largest variety of sites where *tv* sites co-exist with *sv* occupancy. However,

TABLE III. Site occupancy probabilities (%) determined using deposition simulations. The values were collected from 1000 propagations.

M		Zn			Cd			Hg		
RG	*T*, K	*sv*	*tv*	*hv*	*sv*	*tv*	*hv*	*sv*	*tv*	*hv*
Ne	4	0.0	62.3	37.7	0.0	50.9	49.1	0.0	95.8	4.2
	10	0.9	53.1	46.0	0.0	34.0	66.0	0.0	99.7	0.3
Ar	4	100.0	0.0	0.0	87.7	12.3	0.0	100.0	0.0	0.0
	10	100.0	0.0	0.0	90.8	9.2	0.0	100.0	0.0	0.0
Kr	4	100.0	0.0	0.0	97.3	2.7	0.0	100.0	0.0	0.0
	10	99.7	0.3	0.0	97.9	1.9	0.2	100.0	0.0	0.0
Xe	4	100.0	0.0	0.0	100.0	0.0	0.0	100.0	0.0	0.0
	10	100.0	0.0	0.0	100.0	0.0	0.0	100.0	0.0	0.0

even in this system the guest metal atom is trapped mainly (> 90%) in a single vacancy site after sample annealing. The most clear-cut site occupancy is exhibited in xenon matrices where *sv* sites are found exclusively for all three metals. The other system with a propensity for *sv* site occupancy is atomic mercury in the three heavier solids. The specific findings of the simulated depositions are consistent with the qualitative predictions outlined in the Introduction which were based on the simple comparisons presented in Fig. 1 between the nearest neighbor distance for each vacancy sites and the equilibrium position in the RG–M potentials.

No defects were observed out the region occupied by the guest atom. As the RG atoms impact on the template covering randomly the surface, before the last atomic layer is totally covered, RG atoms impact covering the next one. Because of that, defects are only observed in the last two uncovered atomic layers where the metal atom is never present. Accordingly, defects will play no role in the present system in the atomic metal spectroscopy.

3.2. Spectra

3.2.1. Electronic populations

The diabatic states were initially populated equally. The diabatic couplings increase with the excitation of the metal atom and remain high during all the dynamics allowing a continuous transfer of population among the diabatic states. In the diabatic representation, emission takes place from three states leading to a triplet structured band, which is not observed in any of the recorded matrix luminescence experiments.

The adiabatic populations were computed as an average of the 300 overall trajectories for each M/RG system. The behavior of the adiabatic population was found to be quite similar for all systems.

Thus, upon direct excitation all three adiabatic states have the same energy and equal populations. However, as the dynamics evolves the three electronic states diverge, leading to a rapid transfer of population from the highest adiabatic state to the lower ones. For Zn/Ar system, after just 100 fs all of the electronic population has left the highest energy adiabatic level (State 3) while it takes up to 600 fs for complete depopulation of the intermediate level (State 2). At this point all the population has been transferred to the lowest energy adiabatic level (State 1). This very rapid relaxation

(complete in 0.6 ps) demonstrates that fluorescence takes place only from the lowest adiabatic level to the ground state, so that upon photoexcitation, most of the structural characteristics of the systems are determined by the time evolution on this one level. This behavior was observed in all cases where time relaxation increases when the RG weight increases.

As in the case of Hg in RG matrices,[15] hops among electronic states occur in the first ps and the essentials of the excited state dynamics occur on the lowest energy level of the excited PES. As detailed in a forthcoming publication, more refined calculations with MDQT show that the lowest energy excited state is rapidly reached.

3.2.2. Absorption (excitation) spectra

Absorption spectra were computed following the method outlined in Sec. 2. The simulated spectra are presented in Figs. 3, 5–8 where they are compared with the experimental data recorded as excitation spectra by the Maynooth Group. The absorption spectra calculated for each vacancy site in Ne, Ar, Kr and Xe are presented in Fig. 3 for Zn and Cd. The threefold splitting present in the recorded spectra are well reproduced in the simulations. With the exception of neon this effect is observed in all systems considered in this work. It arises as photoexcitation of the metal atom to its degenerate $^1P_1$ electronic state, accesses the three electronic levels correlated to the $J = 1$ state through the projection of the total angular momentum J. As a partial conclusion we point that the role of the different vacancy sites to the absorption is hidden, from the results presented in Fig. 3. The exceptional system is Zn/Ar where, as is evident in Fig. 3, only the *sv* site compares favorably both in terms of location and structure to the recorded band. For the other M/RG systems the simulated absorption spectra for each vacancy type appears in the same energy range as the experimental spectra. The shifted contributions observed for *tv* and *hv* sites in Zn/Ar system could be related to the small band observed at 214 nm in the excitation spectra.[2] This band was recorded for deposited sample and after the annealing it disappears. It means that contribution of *tv* and *hv* sites could correspond to the contributions of the unstable thermal sites observed in the experiment.[2] From a theoretical point of view, the different behavior observed for Zn/Ar system could be related to the fact that in the region of the equilibrium position in ground state, the E potential curve is more repulsive than in the other systems as presented in Fig. 4. The differences observed in the energetic gap between ground and $^1\Sigma$ curves for a *sv* site and *tv* and *hv* sites are bigger in Zn/Ar matrices than in the other analyzed systems.

For neon matrices doped with atomic zinc or cadmium, complex structured absorption bands were consistently observed in the experiment.[1] As is evident in the bottom panel of Fig. 3 structures were partially resolved in Cd/Ne while only a shoulder to the red of the main band was observed for Zn/Ne. Recording excitation spectra of slightly shifted emission bands revealed the complex absorption bands arose from multiple site occupancy (see Fig. 4 and Fig. 8 of Ref. 1, respectively, for Zn/Ne and Cd/Ne). In order to get more insight in the site analysis of the Zn/Ne and Cd/Ne the emission bands of these systems were calculated.

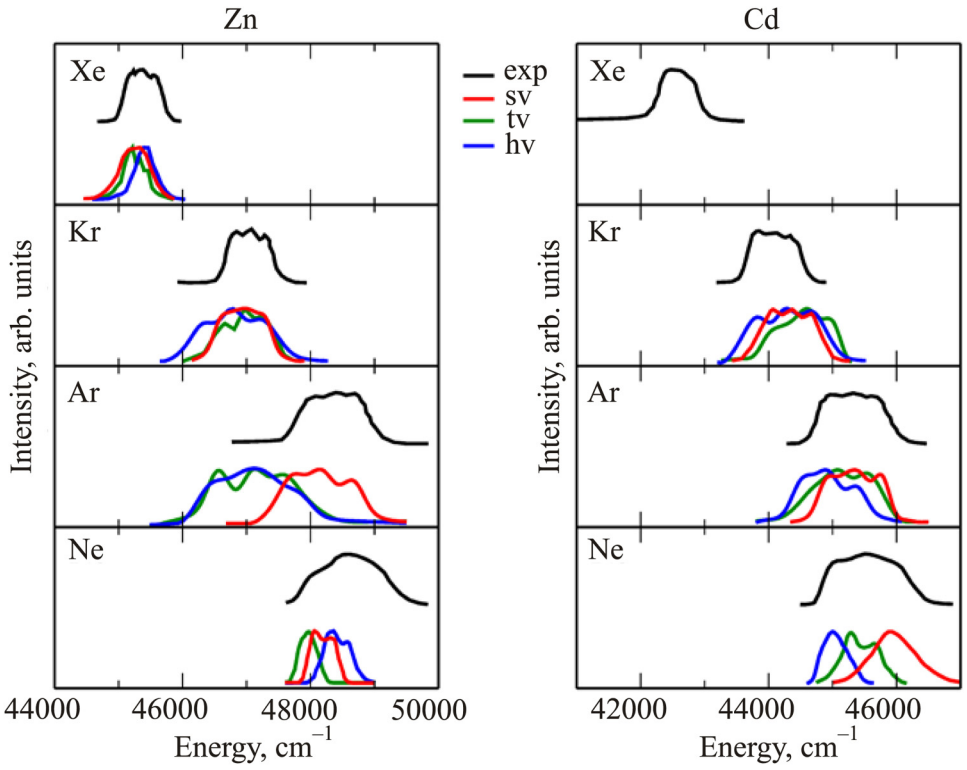

FIG. 3. Absorption bands arising from the $^1P_1 \leftarrow ^1S_0$ transition that takes place for the metal atoms Zn and Cd trapped in four rare gas matrices Ne, Ar, Kr and Xe. On the top of each panel, the experimental bands are represented with black solid lines. The simulated absorption bandshapes of the three sites are shown colour coded —red for *sv*, green for *tv* and blue for *hv* sites.

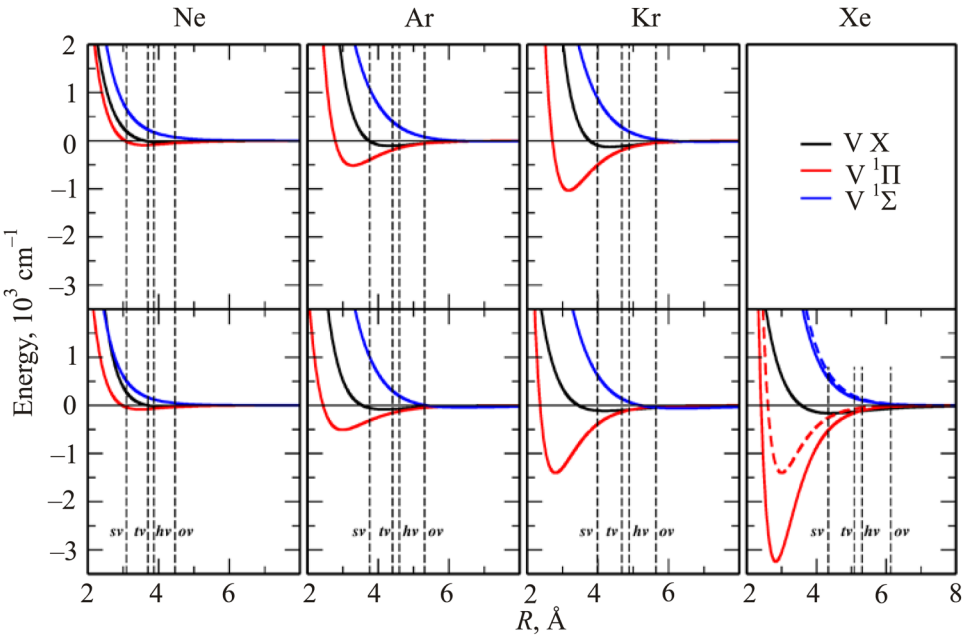

FIG. 4. Interatomic potential curves X, $^1\Pi$ and $^1\Sigma$ for molecular complex 1:1 M–RG. Top panels for Cd/RG and bottom panels for Zn/RG.

3.3.3. Emission spectra

The simulated $^1P_1 \rightarrow {}^1P_1$ emission spectra for these two systems are presented in Fig. 5. As is evident there, the results obtained from the simulations do not reproduce well the bandwidth of the spectra (Fig. 5, bottom panels). This could be related to the quality of the potentials used in the description of $^1P_1$ excited state, the softness of the Ne solid and thus the applicability of the thermal quantum correction applied. Taking into account the abundance of each kind of site (Table III) the contributions of each site to the

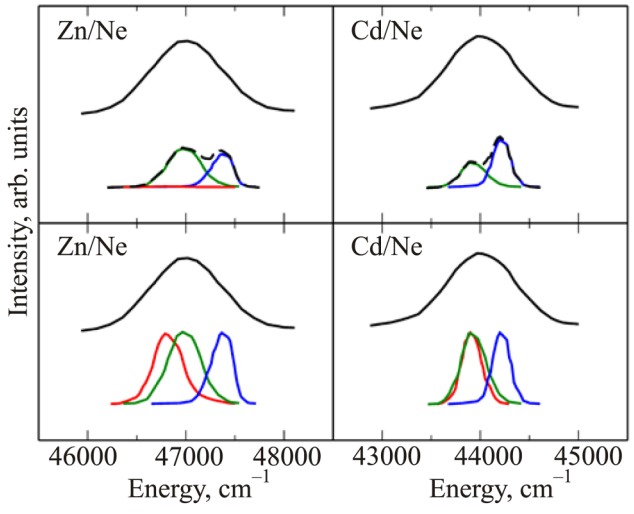

FIG. 5. The emission spectra of $^1P_1 - {}^1S_0$ transition of Zn (left) and Cd (right) atoms trapped in Ne matrices. In both panels the experimental spectra are presented on the top by the black traces. On the bottom the contributions of *sv* (red), *tv* (green) and *hv* (blue) sites obtained from MDQT simulations are shown colour coded. The top panels show the calculated weighted contributions for each site as specified in Table III. The black dashed line corresponds to the weighted sum of all site contributions.

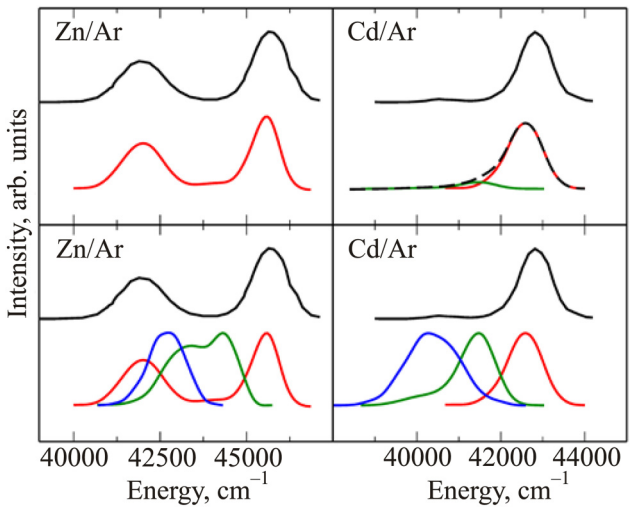

FIG. 6. The emission spectra of $^1P_1 - {}^1S_0$ transition of Zn (left) and Cd (right) atoms trapped in Ar matrices. In all panels on top are presented experimental spectra for annealed samples, and on bottom are shown the contributions of *sv* (red), *tv* (green) and *hv* (blue) sites obtained from MDQT simulations. Top panels show the calculated weighted contributions for each site. The black dashed line corresponds to the weighted sum of all site contributions.

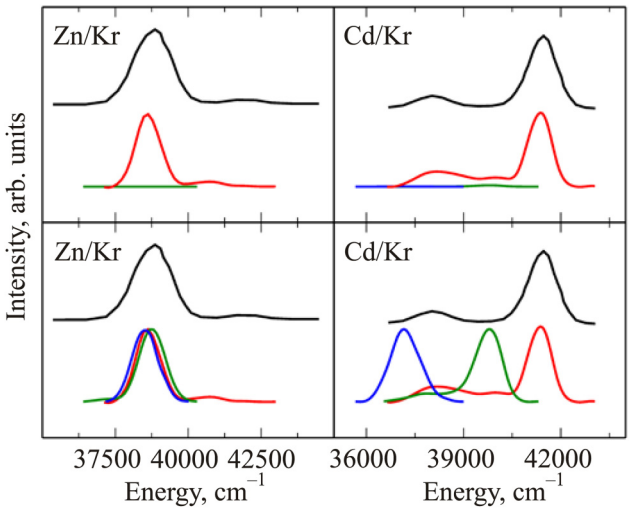

FIG. 7. Simulated emission spectra for the $^1P_1-{}^1S_0$ transition of Zn (left) and Cd (right) atoms trapped in Kr matrices. In all panels on top are presented experimental spectra for annealed samples, and on bottom are shown the contributions of *sv* (red), *tv* (green) and *hv* (blue) sites obtained from MDQT simulations. Top panels show the calculated weighted contributions for each site.

spectra were weighted, the results of which are shown in the top panels of Fig. 5. From Table III one can readily note that *tv* and *hv* sites are predominant. Even applying the weighting procedure, we still cannot reproduce well the shape of the emission spectra and its band width at the half maximum values.

However, the location of the bands is roughly consistent with the small energy shifts observed for the site-related emissions. Moreover, as can be seen in Table IV, the calculated Stokes shift are in good agreement with observed values with the single exception of the Zn/Ne system for which larger difference is found. The origin of such differences between the experimental and theoretical Stokes shifts could reside in the quality of the potential used in the simulations or/and the no applicability of the DIM approximation

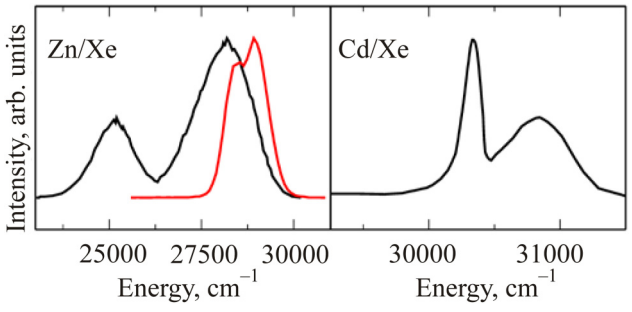

FIG. 8. Experimental (black) and calculated (red) emission bands associated to $^3P_1-{}^1S_0$ photoexcitation of Zn atoms trapped in Xe matrices (left). Experimental emission bands associated to $^1P_1-{}^1S_0$ photoexcitation of Cd atoms trapped in Xe matrices (right).

TABLE IV. Structural and photophysical characteristics of the $^1P_1-{}^1S_0$ emission band for the M/RG matrix systems. The Stokes shift (SS) is calculated as peak-to-peak energy difference.

			SS, cm^{-1}		
System		λ_{em}, nm	Exp.	Calc.	dev.%
Zn	Ne	212.7	1734	1246	28
	Ar	218.9	2696	2583	4
		238.0	6362	6177	3
	Kr	239.5	5327	6183	16
		259.0	8471	8392	1
Cd	Ne	221.7	1567	1550	1
	Ar	233.4	2519	2776	10
	Kr	241.3	2742	3004	10
		262.0	6021	6240	4

for this system. In the case of Zn/Ne no reliable potential exists describing the involved excited states, thus leading to the worst agreement between theory and experiments.

The emission spectra calculated for the three distinct sites in the M/Ar systems are represented in Fig. 6. The different contributions from each site vacancy span the whole emission region for both Zn and Cd as shown in the bottom panels in Fig. 6. When weighted spectra are used, good agreement with experimental data (see top panels in Fig. 6) is found in both systems.

In the case of Ar matrices the *sv* site has the best agreement with the experimental emission spectra. For the Zn/Ar system the *tv* and *hv* contributions are shifted to the red and do not match the experimental bands. This behavior is consistent with that previously noted in the absorption spectra. In the case of Cd/Ar matrices the small experimental emission band shifted to the red is associated with thermally unstable occupancy sites.[4] In the Cd/Ar simulations we observed that *tv* sites are formed at low temperatures and contribute to the small emission band, however when the temperature is increased the population of this site decreases and consequently this band become smaller (Table III). Similar behavior was observed in the experiment after an annealing of the system.[4]

The absorption simulations for Zn and Cd atoms in solid Kr (second panel from top in Fig. 3) indicated that site contributions to the bands are located in the same region as the recorded bands for both metal atoms. As made evident on the left in Fig. 7, the contributions of the three sites to the emission are all located in the same place in the case of Zn. In contrast they are widely spread in the case of Cd as shown in the bottom right panel of Fig. 7.

The weighted contributions for Zn and Cd are shown in the top panels of Fig. 7. In Kr matrices the main contribution is provided by *sv* sites, but also a very small contribution of the *tv* and *hv* sites is observed in Cd/Kr solids (see Table III). It must be pointed out that the pair of emission bands in the Zn/Ar, Zn/Kr and Cd/Kr spectra are not related to multiple site occupancy. In all of these cases the characteristics of the emission spectra are well reproduced with the *sv* sites contributions alone. This result was confirmed in Ref. 2. The two bands could be explained in terms of different dynamical collective modes that are activated in the matrix upon the photoexcitation of the metal atom.[37]

Three different dynamical behaviors were observed in the MDQT simulations. Two of them are the same as those first presented in Ref. 37 and described as "body" and "waist" modes. However, in the current simulations another distinct mode, labelled "no-complex" (NC), was identified. In this mode the metal atom remains in the equilibrium position after its photoexcitation, and six of the twelve nearest neighbors come closer to it than the others, but not as close as occurs in the "body" and "waist" modes. The main contributions to the double emission bands arise from the activation of the body mode (lesser energy emission band) and the NC mode (higher energy emission band). Analysis of the geometries and population of the different collective modes will be fully discussed in the forthcoming paper.

Atomic zinc trapped in solid xenon was the only M/Xe matrix system studied in this work using MDQT due to the unavailability of interatomic potentials describing Cd($^1P_1$)–Xe interactions. This system is extremely interesting because only emission from the $^3P_1$ state is observed when the Zn is photoexcited to its $^1P_1$ electronic state.[1–2] Thus no $^1P_1 - {}^1S_0$ fluorescence was recorded in the experiments[1,2] even at the lowest attainable temperatures of 4 K. The recorded emission spectrum (Fig. 8) shows two resolved bands assigned to the electronic excited state $^3P_1$ with similar bandwidth. In the Cd/Xe system the experiment shows a similar behavior, but in this case the red shifted band is narrower in comparison with the blue shifted one. The presence of the narrow band was assigned, on the basis of the line measured lifetime, to emission from the metastable $^3P_0$ state.[4] However, no explanation has been proposed for the occurrence of two emission bands in the case of Zn/Xe system.

Only *sv* sites were considered in calculations of the absorption and emission bands because in the simulated deposition, only this kind of site was observed to form for both the Zn/Xe and Cd/Xe systems. In Fig. 8 the characteristics of calculated bands and the experimental data are presented. As mentioned earlier simulated spectra cannot be generated in the Cd/Xe system due to the lack of Cd-Xe potentials.

The MDQT simulations applied to study the Zn/Xe system reproduce the absorption band shown in Fig. 3 with only a small deviation. As shown in Fig. 8 the calculated emission band presents a doublet structure consistent with the two emission bands recorded in the experiments. However, the extent of the splitting is much smaller in the simulations than what is observed and no evidence of the red shifted emission band (at 25,000 cm^{-1}) was obtained. Due to the heavy atom effect, the singlet-triplet intersystem crossing is so efficient, that singlet fluorescence is completely quenched and only emission from the triplet state is observed. Because of this, only the dynamics on the (lower) triplet state is performed to get the emission spectrum and to compare to the experiments. The discussion on singlet-triplet crossing in Xe will be fully discussed in the forthcoming paper, where the dynamics in the singlet and in the triplet state will be described.

4. CONCLUSIONS

The spectra arising for the $^1P_1 - {}^1S_0$ transitions of the metal atoms Zn and Cd trapped in RG matrices were studied using classical molecular dynamics and molecular dynamics with quantum transitions methods. The deposition model applied was useful to identify the three vacancy site occupancies: *sv*, *tv* and *hv*, and to determine the population of each kind of vacancy in all the M/RG systems studied. The results obtained for the absorption and emission bands as well as the Stokes shifts for the electronic transitions $^1P_1 \leftrightarrow {}^1S_0$ of atomic zinc and cadmium in rare gas matrices are in good agreement with the experimental data. The shape of absorption spectra for M/Ne systems is related to multiple site occupancy in this host rather than the breakdown of the $^1P_1$ degeneracy due to the Jahn–Teller effect. Multiple trapping sites have also been shown to be present in Cd/Ar, and in all non-annealed samples. However, the pairs of emission band observed in the spectra recorded for Zn/Ar, Cd/Ar and Zn/Kr systems are not related to the trapping of the metal atom in different vacancies in these solids. These two emission bands originate from different collective modes (body, waist and NC) activated in the system after the photoexcitation of the matrix-isolated metal atom, as it will be explained in more detail in a forthcoming paper.

The good agreement found in the simulations of the site-specific spectroscopic bands of the $^1P_1 - {}^1S_0$ transition for the metal atom trapped in RG matrices, allow us to conclude that stationary $^1P_1$ and $^1S_0$ states are well accounted for with a potentials approach. This means that the PESs generated with the diatomics-in-molecules method provide a good description of the M/RG systems in both stationary states. Furthermore, based on the good agreement found between the observed and simulated site-specific absorptions, attributions of the site occupancy have been achieved in this study. As a result of this, dynamical evolution of the $^1P_1$ state in the M/RG systems will be explored using this approach with the aim of explaining the presence of pairs of emission bands for the $^1P_1 \rightarrow {}^1S_0$ transition for atoms occupying a single vacancy site in the solid rare gases.

ACKNOWLEDGMENTS

This research was supported by the Cuban Ministry of Science through the PNCB P223LH001-108 Programme.

REFERENCES

[1]B. Healy, P. Kerins, and J. G. McCaffrey, Fiz. Nizk. Temp. **38**, 860 (2012) [Low Temp. Phys. **38**, 679 (2012)].
[2]V. A. Bracken, P. Gurtler, and J. G. McCaffrey, J. Chem. Phys. **107**, 5290 (1997).
[3]V. A. Bracken, P. N. Kerins, P. Gurtler, and J. G. McCaffrey, J. Chem. Phys. **107**, 5300 (1997).
[4]B. Healy and J. G. McCaffrey, J. Chem. Phys. **110**, 3903 (1999).
[5]P. Kerins, B. Healy, and J. G. McCaffrey, Fiz. Nizk. Temp. **26**, 1016 (2000) [Low Temp. Phys. **26**, 756 (2000)].
[6]M. E. Fajardo, J. Chem. Phys. **98**, 110 (1993).
[7]M. Ryan, M. Collier, P. de Pujo, C. Crepin, and J. G. McCaffrey, J. Phys. Chem. A **114**, 3011 (2010).
[8]E. Jacquet, D. Zanuttini, J. Douady, E. Giglio, and B. Gervais, J. Chem. Phys. **135**, 17450301 (2011).
[9]R. Fraenkel and Y. Haas, Chem. Phys. **186**, 185 (1994).
[10]R. Fraenkel and Y. Haas, Chem. Phys. Lett. **220**, 77 (1994).
[11]C. Crepin, P. de Pujo, B. Bouvier, V. Brenner, and P. Millie, Chem. Phys. **272**, 243 (2001).
[12]R. Fraenkel, D. Schweke, Y. Haas, F. Molnar, D. Horinek, and B. Dick, J. Phys. Chem. A **104**, 3786 (2000).
[13]A. Kyrychenko and J. Waluk, J. Chem. Phys. **119**, 7318 (2003).

[14]A. Gutiérrez-Quintanilla, M. Chevalier, R. Platakyte, J. Ceponkus, G. A. Rojas-Lorenzo, and C. Crépin, Phys. Chem. Chem. Phys. **20**, 12888 (2018).
[15]G. Rojas-Lorenzo, J. Rubayo-Soneira, S. F. Alberti, and M. Chergui, J. Phys. Chem. A **107**, 8225 (2003).
[16]J. C. Tully, J. Chem. Phys. **93**, 1061 (1990).
[17]J. G. McCaffrey, D. Bellert, A. W. Leung, and W. Breckenridge, Chem. Phys. Lett. **302**, 113 (1999).
[18]E. Czuchaj and M. Krośnicki, Chem. Phys. Lett. **335**, 440 (2001).
[19]W. H. Breckenridge, M. D. Morse, and J. G. McCaffrey, J. Chem. Phys. **109**, 3137 (1998).
[20]D. J. Funk, A. Kvaran, and W. H. Breckenridge, J. Chem. Phys. **90**, 2915 (1989).
[21]M. Strojecki, M. Krośnicki, M. Lukomski, and J. Koperski, Chem. Phys. Lett. **471**, 29 (2009).
[22]K. Yamanouchi, S. Isogai, M. Okunishi, and S. Tsuchija, J. Chem. Phys. **88**, 205 (1988).
[23]J. Zúñiga, A. Bastida, A. Requena, N. Halberstadt, and J. A. Beswick, J. Chem. Phys. **98**, 1007 (1993).
[24]M. Okunishi, H. Nakazawa, K. Yamanouchi, and S. Tsuchija, J. Chem. Phys. **93**, 7526 (1990).
[25]N. W. Ashcroft and N. D. Mermin, *Solid State Physics* (Holt, New York, 1976).
[26]J. Koperski and M. Czajkowski, Phys. Rev. A **62**, 012505 (2000).
[27]M. Strojecki, M. Krosnicki, and J. Koperski, J. Mol. Spectrosc. **256**, 128 (2009).
[28]E. Czuchaj, M. Krosnicki, and H. Stoll, Chem. Phys. **265**, 291 (2001).
[29]J. G. Kaup and W. H. Breckenridge, J. Phys. Chem. **99**, 13701 (1995).
[30]E. Czuchaj and H. Stoll, Chem. Phys. **248**, 1 (1999).
[31]M. Strojecki, M. Krośnicki, and J. Koperski, Chem. Phys. Lett. **465**, 25 (2008).
[32]V. S. Batista and D. F. Coker, J. Chem. Phys. **105**, 4033 (1996).
[33]V. S. Batista and D. F. Coker, J. Chem. Phys. **106**, 6923 (1997).
[34]G. Rojas-Lorenzo, J. Rubayo-Soneira, and S. F. Alberti, Chem. Phys. **362**, 34 (2009).
[35]J. P. Bergsma, P. H. Berens, K. R. Wilson, D. R. Fredkin, and E. J. Heller, J. Chem. Phys. **88**, 612 (1984).
[36]L. Uranga-Piña, A. Martínez-Mesa, J. Rubayo-Soneira, and G. Rojas-Lorenzo, Chem. Phys. Lett. **429**, 450 (2006).
[37]P. N. Kerins and J. G. McCaffrey, J. Chem. Phys. **109**, 3131 (1998).

Translated by AIP Author Services